Extended Nodal Admittance Matrix Based Stability Analysis of HVDC Connected AC Grids

YONGGANG ZHANG[ID][1]**, (Member, IEEE), DANIEL DUCKWITZ**[ID][1,2]**, NILS WIESE**[1]**, AND MARTIN BRAUN**[ID][1,2]**, (Senior Member, IEEE)**

[1]Department of Energy Management and Power System Operation, University of Kassel, 34121 Kassel, Germany
[2]Fraunhofer Institute for Energy Economics and Energy System Technology (IEE), 34117 Kassel, Germany

Corresponding author: Yonggang Zhang (yonggang.zhang@uni-kassel.de)

ABSTRACT Motivated by emerging HVDC oscillation issues resulted from the interaction with AC grids, impedance-based stability analysis has become an attractive approach in the de-risking studies due to the capability of black-box modelling and clear physical meaning. However, impedance-based stability assessment of HVDC is typically conducted either from the AC side or from the DC side, without fully considering both AC and DC grid dynamics, thus impairs evaluation accuracy. In this paper, the nodal admittance matrix based resonance mode analysis method is extended to include both AC and DC dynamics through formulating a hybrid AC/DC nodal admittance matrix. In contrast to the widely adopted Nyquist-based methods, the dynamic mode identification and damping ratio extraction using the frequency scanning of modal impedances derived from nodal admittance matrix is more straightforward for stability check, and the eigenvalue-decomposition based participation factor analysis is more useful in analyzing system wide dynamic interaction and identifying oscillation sources, which is in favor of the design of mitigation measures. The effectiveness of the described method is illustrated by case studies using a simple hybrid AC/DC grid consisting of converter-interfaced generation, synchronous machine and HVDC. Stability impacts of the strengths and modelling details of the connected AC grids for HVDC, the switching states of parallel AC line(s) for HVDC, and different modulation modes of HVDC converters are analyzed. It is observed, the AC-DC dynamic coupling can induce the interaction of the AC grids connected in different HVDC terminals. EMT-simulations in MATLAB/Simulink validate the analytical results.

INDEX TERMS AC-DC dynamic coupling, dynamic mode, damping ratio, HVDC, stability assessment.

I. INTRODUCTION

In order to achieve massive grid integration of renewable energy sources (RES) and long distance power transmission, multiple HVDC links have been constructed and integrated into German grids [1], [2]. Since both HVDC and RES are converter-interfaced components, the fast growth of such power electronics devices in modern power systems have resulted new dynamics and stability issues, and the most commonly encountered one is the wideband resonance stability [3]–[5]. Over the last decade, a series of oscillation incidents involving HVDC have been reported [6], [7].

The recorded oscillation frequencies range from several Hz to above 1 kHz. Typically they are triggered by the change of operating conditions in involved systems [3], [4], [8], such as the grid topology change induced by grid disturbances.

To reveal the mechanisms of such issues and prevent them happening again, e.g. through adopting proper measures in power system planning or operation stages, quite a few studies have been conducted, either through electromagnetic transient (EMT) analysis or analytical stability assessment [4], [7], [8]. Although EMT analysis can usually give plausible stability evaluation results through applying detailed nonlinear grid models, EMT simulation is in most cases time-consuming and incapable of capturing the underlying mechanism of oscillation phenomenon, thus will mainly be

The associate editor coordinating the review of this manuscript and approving it for publication was Dragan Jovcic[ID].

used for validation in the paper [9]. As for the analytical stability assessment, several widely used methods are: state-space based method, Nyquist based method and nodal-based Resonance Mode Analysis (RMA) method [5], [10]. For easy understanding, the nodal-based RMA method will be named as Ybus based method. Both Nyquist and Ybus based methods are impedance methods, which are more popular than state-space based method due to the strengths in natural association with physical circuits and the capability of black-box modelling. However, their application in the stability assessment of HVDC and the resulted hybrid AC/DC grids is typically conducted either in AC side or DC side while partly neglecting or simplifying the dynamics of AC and DC side grids [11]–[14], which may fail to identify the potential arising stability problems when the AC-DC dynamic coupling is strong.

In order to get more complete model for hybrid AC/DC grids including detailed AC and DC grid dynamics that have been partly neglected or simplified in the past, multi-port admittance model of HVDC converter that reserves the AC-DC dynamic coupling has been developed [15], [16] and furtherly applied in enhanced Nyquist based stability analysis [17], [18]. However, these methods fail to identify the critical dynamic modes and the participation factors (PFs) of grid components, which hinders the identification of risk sources. This issue was properly treated in the Ybus based method, which uses nodal admittance matrix for stability assessment [19]. But Ybus based method is typically applied to single sequence component system, which neglects the coupling between positive- and negative-sequence impedances [20]. Moreover, the integration of AC-DC dynamic coupling into Ybus based method has not been found in literatures so far. To bridge the above gaps, this paper extends the traditional Ybus based method to integrate full dynamic couplings and analyzes various stability impacts in hybrid AC/DC grids, simultaneously contributing to accurate stability assessment and better support in mitigation design.

The rest of this paper is organized as follows: Section II compares existing stability analysis methods and introduces the proposed enhancement. Section III presents the test grid including the detailed nonlinear model and the small-signal modelling. Section IV shows the effectiveness of the proposed method through case studies. Section V concludes the work.

II. LIMITATIONS IN EXISTING STABILITY ANALYSIS METHODS AND THE PROPOSED ENHANCEMENT

Figure 1. (a) shows a simple hybrid AC-DC grid with embedded HVDC, synchronous machine (SM) and renewable energy source (RES). Two-level voltage-source converter (VSC) based HVDC is adopted in the study. The HVDC is parallel with a high-voltage AC (HVAC) branch. Figure 1. (b) shows the RES and the feeding route, e.g. for representing the application of wind park integration. An aggregated single-converter model was adopted.
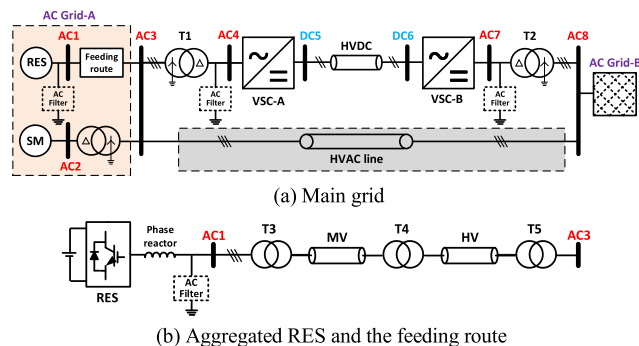

(a) Main grid

(b) Aggregated RES and the feeding route

FIGURE 1. Hybrid AC-DC grid with embedded HVDC, SM and RES.

Multiple converter-interfaced components and controllers are involved in the system, with the potential for stability-critical interactions. For the stability check of such a test grid, the most widely used analytical methods including the state-space based method, Nyquist based method and Ybus based method are compared in TABLE 1. Limitations of the compared methods regarding the state-of-the-art are marked with red letters. Some disadvantages are marked with orange letters.

TABLE 1. Comparison of small-signal stability analysis tools.

Methods → Features ↓	State-space based method	Nyquist based methods	Ybus based method
System representation	State-space equation	Source-load impedances	Node-voltage equation
Domain	Time	Frequency	Frequency
Scalability [5]	Low	Middle	High
Stability criterion	All eigenvalues in LHP[a]	NC[b] / GNC[b] (Number of RHP[a] poles required)	All modal resistances positive
Input-output dynamics	✓	✓	✓
Black-box modelling	✗	✓	✓
Asymmetrical control coupling	✓	✓	✗ (enhanced in this paper)
AC-DC dynamic coupling	✓	✓	✗ (enhanced in this paper)
Dynamic modes & PFs	✓	✗	✓

a. LHP = Left half-plane, RHP = Right half-plane; b. NC=Nyquist criterion, GNC = Generalized NC

For the state-space based method, it requires detailed information on the circuit, control and parameters of a system to build system state-space model, which is naturally incapable of black-box modelling and lack of scalability [5], [21]. While for the Nyquist based methods, it is shown in [10] that bode plots can not predict system stability accurately under certain conditions and Nyquist diagrams are not straightforward in checking the right-half plane (RHP) poles and the encirclements of (-1, 0). Moreover, when checking the stability of strongly meshed AC/DC grids using Nyquist based methods, it is difficult to partition the system into source-load subsystems at any point and it may require the stability check at multiple partitioning points [14], which weakens the suitability of the method for complex systems.

As for the Ybus based method, it has the best scalability but lacks the integration of asymmetrical control coupling and AC-DC dynamic coupling regarding the state-of-the-art. To simultaneously achieve accurate stability check and stability risk localization for a hybrid AC/DC grid, the Ybus based method will be enhanced to eliminate its limitations as listed in TABLE 1.

As the basis for enhancement, the nodal admittance matrix of the test system should be formulated, and before that, all components should be modelled as parallel or series admittance networks. To integrate the dynamic coupling induced by asymmetrical converter control in admittance modelling, the AC side of grid components should include positive- and negative-sequence ports when modelled in the natural reference frame, or d- and q-axis ports when modelled under dq-frame [7]. The sequence ports and dq ports can be equivalently transformed to each other through linear transformation and frequency shifting [7]. For the convenience of determining the PFs of d- and q-control loops in the critical dynamic modes, the dq-frame modelling is selected. With the objective of integrating AC-DC dynamic coupling in admittance modelling, each HVDC converter is modelled as a three port hybrid AC/DC admittance network, with two ports at AC side and one port at DC side [17]. Then the SM, RES, AC filters and external grid (as parallel AC grid components) are modelled as two port admittance network. The AC lines and transformers (as series AC grid components) are modelled as four port admittance network. The HVDC cable (as a series DC grid component) is modelled as a two port admittance network.

Since the admittance modelling of active components including SM, RES and HVDC converter is locally linearized, which depends on the angle of the local reference frame, the models developed under local reference frames will be rotated to a defined global reference frame [14]. Note that the modelling of DC components and DC ports of hybrid AC/DC components does not involve dq-frame rotations. In addition, the stationary frame in DC side can be mapped to the dq-frame of AC side without frequency shifting. On this basis, all components can be directly connected in circuits for system level analysis. Nodal admittance matrix of the studied system is formulated in (1), as shown at the bottom of the page, where i_{AC1} and I_{DC5} denote the current source injections to the nodes AC1 and DC5, u_{AC1} and U_{DC5} denote

the voltages of AC1 and DC5, Y_{11} and Y_{55} denote the nodal admittances of AC1 and DC5, and other terms follow the same notation.

In comparison to the commonly used nodal admittance matrix that is formulated using single phase or sequence component variables, the nodal current of each AC node in (1), e.g. i_{AC1}, is a column vector comprised of d- and q-axis currents under global reference frame, e.g. as denoted by I_{d1} and I_{q1}. Each AC admittance element in the nodal admittance matrix is a 2-order matrix instead of a single quantity. The integration of DC grid nodes in the node-voltage equation gives a hybrid AC-DC nodal admittance matrix.

Having L_K and T_K as the left and right eigenvector matrices of Y_{KK} obtained through matrix decomposition [22], the eigenvalue admittance matrix Y_M of Y_{KK} is also obtained, as illustrated in Figure 2. Through setting $i_M = T_K i_K$ and $u_M = T_K u_K$, the system $i_K = Y_{KK} u_K$ in nodal coordinate system can be transformed to $i_M = Y_M u_M$ in modal coordinate system. Then inversing the modal admittance matrix Y_M yields the modal impedance matrix

$$Z_M = Y_M^{-1} = L_K Y_{KK}^{-1} T_K \tag{2}$$

where $L_K = T_K^{-1}$. Performing frequency scanning to the frequency-dependent modal impedances $Z_{m1}(s)$, $Z_{m2}(s)$, $\ldots, Z_{mn}(s)$, i.e. the diagonal terms of Z_M, the critical dynamic modes can be determined by the peaks of the impedance amplitude versus frequency curves, which is the basis concept of resonance mode analysis (RMA) [19]. The frequencies at curve peaks indicate the frequencies of dynamic modes. The stability of the kth dynamic mode can firstly be checked by the real part value of the corresponding complex-valued modal impedance at the oscillation frequency f_k, i.e. the $R(f_k)$ of

$$Z_{mn}(f_k) = R(f_k) + jX(f_k) \tag{3}$$

if $R(f_k) < 0$, the dynamic mode is unstable due to negative damping while the dynamic mode is stable if $R(f_k) > 0$ due to positive damping, and the damping ratio ξ_k can be defined as

$$\xi_k = \frac{1}{2Q_k} = \frac{\Delta f_k}{2f_k} \tag{4}$$

where Q_k denotes the quality factor of kth resonance circuit, as defined by the frequency-to-bandwidth ratio of the

$$\underbrace{\begin{bmatrix} i_{AC1} \\ i_{AC2} \\ i_{AC3} \\ i_{AC4} \\ I_{DC5} \\ I_{DC6} \\ i_{AC7} \\ i_{AC8} \end{bmatrix}}_{i_K} = \underbrace{\begin{bmatrix} Y_{11} & 0_{2\times2} & Y_{13} & 0_{2\times2} & 0_{2\times1} & 0_{2\times1} & 0_{2\times2} & 0_{2\times2} \\ 0_{2\times2} & Y_{22} & Y_{23} & 0_{2\times2} & 0_{2\times1} & 0_{2\times1} & 0_{2\times2} & 0_{2\times2} \\ Y_{31} & Y_{32} & Y_{33} & Y_{34} & 0_{2\times1} & 0_{2\times1} & 0_{2\times2} & Y_{38} \\ 0_{2\times2} & 0_{2\times2} & Y_{43} & Y_{44} & y_{45} & 0_{2\times1} & 0_{2\times2} & 0_{2\times2} \\ 0_{1\times2} & 0_{1\times2} & 0_{1\times2} & y_{54} & Y_{55} & Y_{56} & 0_{1\times2} & 0_{1\times2} \\ 0_{1\times2} & 0_{1\times2} & 0_{1\times2} & 0_{1\times2} & Y_{65} & Y_{66} & y_{67} & 0_{1\times2} \\ 0_{2\times2} & 0_{2\times2} & 0_{2\times2} & 0_{2\times2} & 0_{2\times1} & y_{76} & Y_{77} & Y_{78} \\ 0_{2\times2} & 0_{2\times2} & Y_{83} & 0_{2\times2} & 0_{2\times1} & 0_{2\times1} & Y_{87} & Y_{88} \end{bmatrix}}_{Y_{KK}} \underbrace{\begin{bmatrix} u_{AC1} \\ u_{AC2} \\ u_{AC3} \\ u_{AC4} \\ U_{DC5} \\ U_{DC6} \\ u_{AC7} \\ u_{AC8} \end{bmatrix}}_{u_K} \tag{1}$$

resonance circuit, and Δf_k denotes the resonance bandwidth at half maximum, which is the difference between the two neighbored frequencies (of f_k) at which the impedance amplitudes are equal to half of the peak amplitude value (at f_k) [23]. The other common nearly equivalent definition for Q is the ratio of the energy stored in the oscillating resonance circuit to the energy dissipated per cycle by damping processes [23].

After identifying critical dynamic modes, the system can be transformed from modal coordinate system back to nodal coordinate system, as illustrated in Figure 2. The eigenvector matrix T_K or L_K can be used to determine the PFs of both AC and DC grid nodes for the dynamic modes. An alternative way of dynamic mode identification and stability assessment is to evaluate the poles of the closed loop system [24], [25]

$$u_K = Y_{KK}^{-1}(s)i_K \tag{5}$$

taking the nodal current vector i_K as input and the bus voltage vector u_K as output, i.e. solving

$$\det[Y_{KK}(s)] = 0 \implies s_k = \sigma_k + j\omega_k (k = 1, 2, \ldots, n) \tag{6}$$

where σ_k is the attenuation factor of the mode and $\omega_k = 2\pi f_k$ is the oscillation angular frequency. The damping ratio ξ_k can be defined as

$$\xi_k = \frac{-\sigma_k}{\sqrt{\sigma_k^2 + \omega_k^2}} \tag{7}$$

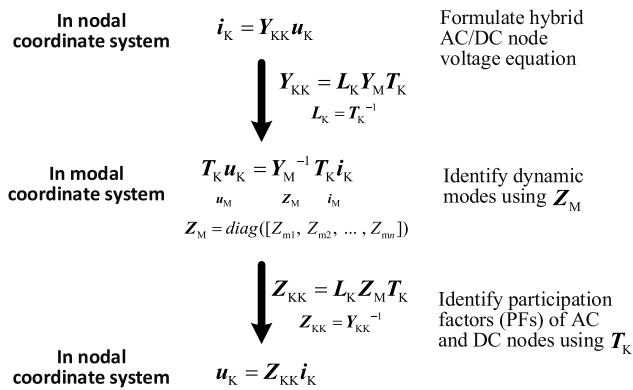if $\sigma_k > 0$, the dynamic mode is unstable.

FIGURE 2. Schematic diagram of resonance mode analysis (RMA).

Note that the real part $R(f_k)$ of modal impedance in (3), in which the Laplace operator s is an imaginary value, and the attenuation factor σ_k of the closed system pole in (6), in which s is a complex value, are complete different quantities, which should not be mixed up in the formulation of damping ratio.

Moreover, finding the poles of closed loop system transfer function through solving the roots of $\det[Y_{KK}(s)] = 0$ requires that each element of the matrix $Y_{KK}(s)$ is given in the form of continuous function of frequency [26], which is not the case as illustrated in Appendixes A-C, thus the point-by-point numerical manipulation over frequency and the approximation, e.g. by vector fitting [27], on each set of

frequency response by a continuous function of frequency is needed, which is a major disadvantage of this approach. Furthermore, due to the better visualization and physical meaning of impedance versus frequency curves in dynamic mode identification than the poles of closed-loop transfer function, only the (modal impedance) frequency scanning method as illustrated in Figure 2 and Eq. (2)-(4) will be considered for further analysis.

III. GRID MODEL

The 8-bus grid in Figure 1 is adopted for analysis. The component models and their main parameters are given in TABLE 2. For the SM, the detailed round rotor synchronous machine model from MATLAB/Simscape library is adopted [28]. For the RES, the virtual synchronous machine (VSM) control, as one of the grid-forming (GFM) control methods, is adopted, as shown in Figure 3. The readers are referred to [29] for the details on the design of the VSM. For the HVDC, the generally used grid-following (GFL) control in real applications is adopted. Detailed circuit and control diagrams of the HVDC converters are shown in Figure 4.

GFL converters use phase-locked loop (PLL) to synchronize with grid, while the GFM converter automatically synchronize with grid through the swing blocks in VSM core, as shown in Figure 3 and Figure 4 individually. For the transformers, the typically used T model is considered, the series branch is described by the short-circuit voltage expressed in percentage (u_r as resistive part and u_x as inductive part), and the shunt magnetizing branch is described by paralleled resistance and inductance, both of which are set as 500 pu [7].

With the above configuration, the interaction of GFL converter, GFM converter and SM is involved in the test system. To prepare for the stability analysis, the dq-frame admittance models of SM and RES are derived referring to [30], as presented in Appendix A and Appendix B. Similarly, the three-port admittance modelling of HVDC converters through combining the control and power stage equations (including the AC-DC power balance) is conducted and validated through EMT simulations, as presented in Appendix C. Note that two DC voltage compensation modes for the modulation of HVDC converters are commonly seen in literatures [18], [31], as distinguished by constant DC voltage U_{dc0} compensation and instantaneous DC voltage u_{dc} compensation, as shown in in Figure 4. Both modes will be considered to show their impact on stability assessment.

IV. CASE STUDIES

After validating the derived admittance models of RES, SM and HVDC converters, the nodal admittance matrix of the test grid can be formulated through connecting the grid components into circuits and used for verifying the effectiveness of the proposed method. An overview of the case studies is given in TABLE 3.

TABLE 2. Brief description and main parameters of the grid model.

| Generations	RES: 650 V, 1.4 GVA, SM: 27 kV, 1.4 GVA (see Appendix A and B for detailed models and paras)
HVDC converter	400 kV (AC) / ±350 kV (DC), 1 GW (see Appendix C for detailed models and parameters)
HVDC line	100 km DC cable (π model) : $R = 0.0139 \ \Omega/\text{km}, L = 0.159 \ \text{mH/km}, C = 231 \ \text{nF/km}$
HVAC line	double AC lines, 100 km, π model: $R = 0.025 \ \Omega/\text{km}, L = 0.796 \ \text{mH/km}, C = 14 \ \text{nF/km}$
Transformer T1,T2	400 / 400 kV, 1 GVA, $u_\text{r} = 0.18\%, u_\text{x} = 16.4\%$
Transformer T3	20 / 0.65 kV, 1.5 GVA, $u_\text{r} = 1\%, u_\text{x} = 4\%$
Transformer T4	110 / 20 kV, 1.5 GVA, $u_\text{r} = 0.6\%, u_\text{x} = 12\%$
Transformer T5	400 / 110 kV, 1.5 GVA, $u_\text{r} = 0.18\%, u_\text{x} = 16.4\%$
HV line - 110 kV	$R = 0.04 \ \Omega, L = 0.414 \ \text{mH}$ (lumped RL model)
MV line - 20 kV	$R = 0.001 \ \Omega, L = 3.82 \ \mu\text{H}$ (lumped RL model)
AC Grid-B	Thevenin circuit with X/R = 50 and variable capacity
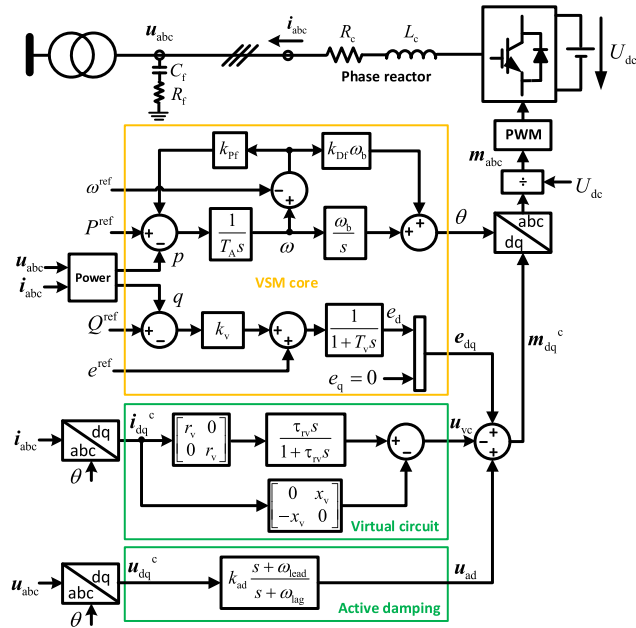
FIGURE 3. Circuit and control diagram of the adopted VSM-based RES.

TABLE 3. An overview of the case studies.

Case A)	Stability impact of weak grid connections for HVDC
Case B)	Stability impact of different DC voltage compensation modes for the modulation of HVDC converters
Case C)	Stability impact of the switching states of (single or double) parallel AC line(s) for HVDC
Case D)	Stability impact of SM/RES in contrast to a simplified Thevenin circuit with same short circuit capacity

A. STABILITY IMPACT OF WEAK GRID CONNECTION

Firstly, the simplified grid as shown in Figure 5 is adopted for analysis. The AC Grid-A and AC Grid-B are both modelled as ideal voltage sources with series RL impedances, and they are characterized by the short circuit ratios of SCR-A and SCR-B. The X/R ratio of their RL impedances is fixed to 50.
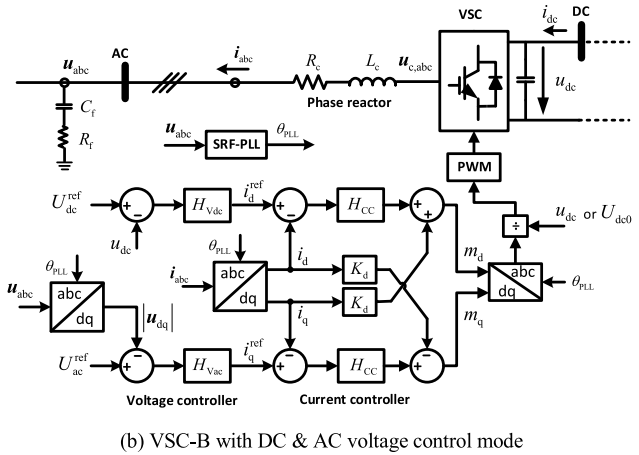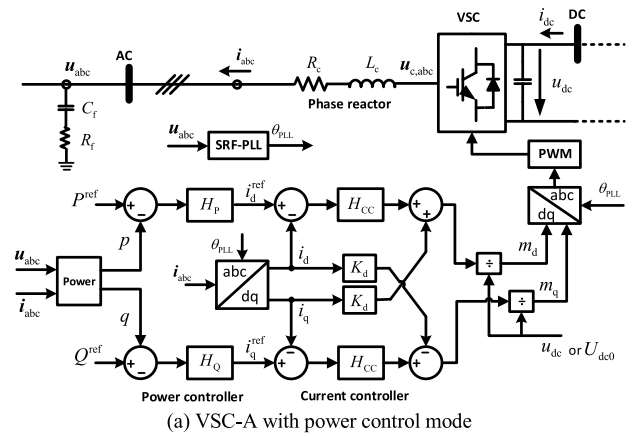

(a) VSC-A with power control mode

(b) VSC-B with DC & AC voltage control mode

FIGURE 4. Circuit and control diagram of the HVDC system.

The left side HVDC converter is operated in the active power control mode, and its setpoint is set as $P = 0.6$ pu. The right side HVDC converter is operated in the DC voltage control mode. Both converters adopt the instantaneous DC voltage (u_dc) compensation. Initially, both SCR-A and SCR-B are set to 4, i.e. the short circuit capacities of AC Grid-A and AC Grid-B are 4 GVA, then they are reduced to 2 to show the stability impact of weak grid.

Frequency scanning of the resulted modal impedances $Z_{m1}(s), Z_{m2}(s) \ldots Z_{mn}(s)$ for SCR-A=2 and SCR-B=2 are presented in Figure 6. Curve peaks in the amplitude plot indicate dynamic/resonance modes, and the corresponding values in the real part plot indicate if the damping is positive or negative. For simple illustration, only two critical dynamic modes at around 7 Hz and 18 Hz are shown, as indicated by the orange and green solid lines for the instantaneous DC voltage (u_dc) compensation mode. Note that the green solid line partly overlap with the blue dashed line. The positive damping of the 7 Hz resonance mode indicates a damped oscillation and the damping ratio is around $\xi_k = 0.7\text{Hz} / (2 \times 7 \ \text{Hz}) = 0.05$ according to (4). The negative damping of the 18 Hz resonance mode indicates an undamped oscillation, as validated in Figure 7 (a). Note that the unstable resonance mode from

analytical results matches the sustaining oscillation wave-form due to the controller saturation as oscillation grows.
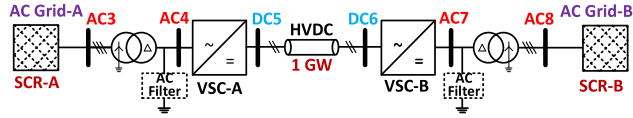

FIGURE 5. Simplification to the test grid in Fig.1: replacing AC Grid-A with a Thevenin circuit and disconnecting the AC transmission line.

FIGURE 6. Modal impedances by SCR-A=2 and SCR-B=2 for VSC-A with udc compensation (solid lines) and Udc0 compensation (dashed lines).

(a) VSC-A with u_{dc} compensation

(b) VSC-A with U_{dc0} compensation

FIGURE 7. EMT simulation validation of modal analysis for weak grids.

TABLE 4. Node PFs (%) for different DC voltage compensation modes.

PF in %	AC3-d/q	AC4-d/q	DC5	DC6	AC7-d/q	AC8-d/q
VSC-A with u_{dc} compensation ↓						
7 Hz Mode	14/ **23**	23 / **40**	0	0	0	0
18 Hz Mode	0 / 0	0 / 0	8	8	**38** / 15	**22** / 9
VSC-A with U_{dc0} compensation ↓						
7 Hz Mode	14 / **23**	24 / **39**	0.1	0.1	0.3 / 0.2	0.2 / 0.1
18 Hz Mode	**3** / 0	**4** / 0	7	7	23 / **28**	13 / **15**

Node participation factors for each resonance mode (total value is 100 in %) are presented in TABLE 4, from which

the domination of the 7 Hz mode by the q-ports of AC3 and AC4, and the domination of the 18 Hz mode by the d-ports of AC7 and AC8 are identified. In other words, the 7 Hz mode is induced by the interaction of the left side HVDC converter (VSC-A) with the weak grid connection (AC Grid-A), mainly involving the q-control loop (including PLL) of VSC-A, while the 18 Hz mode is induced by the interaction of the right side HVDC converter (VSC-B) and the weak grid connection, mainly involving the d-control loop of VSC-B. The contributions of DC nodes to the 18 Hz mode are also indicated by the PFs of the nodes DC5 and DC6. However, the instantaneous DC voltage (u_{dc}) compensation in VSC-A blocks the propagation of the 18 Hz oscillation from AC Grid-B to AC Grid-A.

B. STABILITY IMPACT OF DC VOLTAGE COMPENSATION MODE

DC voltage compensation using either the constant value U_{dc0} or the instantaneous value u_{dc} is widely used in converter modulation [18], [31]. For the PQ-controlled HVDC converter (VSC-A), replacing instantaneous u_{dc} compensation with constant U_{dc0} compensation mainly influences the 7 Hz resonance mode, as indicated by the modal impedances shown in Figure 6. For the U_{dc0} compensation mode, the damping of the 7 Hz resonance (red dashed line) is positive and the damping ratio is around $\xi_k = 1\text{Hz} / (2 \times 7 \text{Hz}) \approx 0.07$ according to (4), which is slightly larger than the damping ratio of the u_{dc} compensation mode around 0.05, as calculated in Section IV.C. For simplicity, this statement can be qualitatively obtained by looking at the sharpness of the amplitude curve peaks. A less sharped amplitude peak indicates larger damping ratio, which can be validated by comparing the EMT simulation results in Figure 7 (a) and (b). Another observation form the EMT- simulation in Figure 7 (b) is, the sending end 7 Hz waveform (blue line) in the time range of 3-4 s is superimposed by the 18 Hz oscillation component in the time range of 4-5 s. And this phenomenon can be furtherly explained by the node PF analysis as shown in TABLE 4. When VSC-A adopts U_{dc0} compensation, the AC Grid-A side nodes also participate the 18 Hz resonance mode, besides, the AC Grid-B side nodes have slight participation in the 7 Hz resonance mode. The observed phenomenon clearly reflects the AC-DC dynamic coupling.

C. STABILITY IMPACT OF THE PARALLEL AC LINE FOR HVDC

As already shown in above subsections, the simplified test grid in Figure 5 is stable at SCR-A=4 and SCR-B=4, and becomes unstable when SCR-B is reduced to 2. If increasing SCR-A to 6 and keeping SCR-B as 2, the overall SCR of the HVDC connections is still 8. Under this condition, it will be checked if the 18 Hz resonance mode can be stabilized by connecting the parallel AC line for HVDC. Then the new test grid is illustrated by Figure 8.

Figure 9 shows the modal impedances considering the following Scenarios: (a) no AC line connection; (b) single
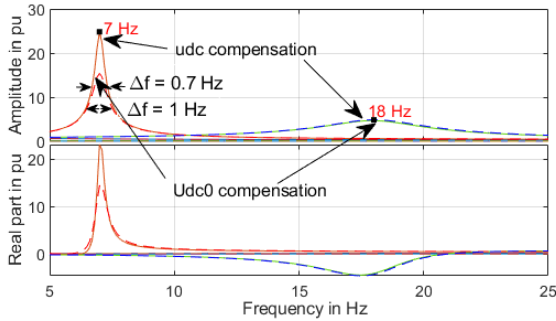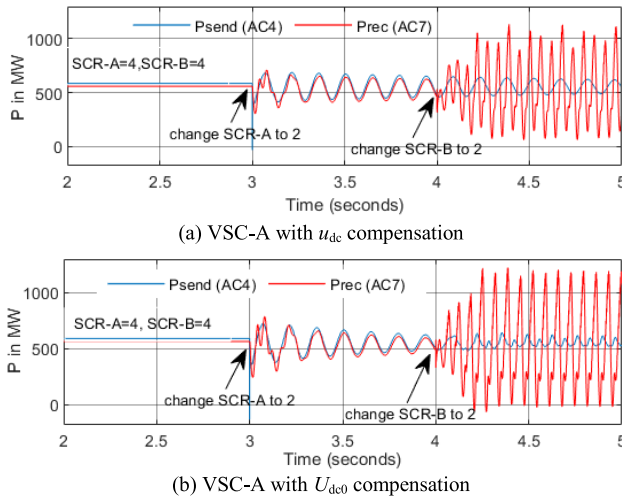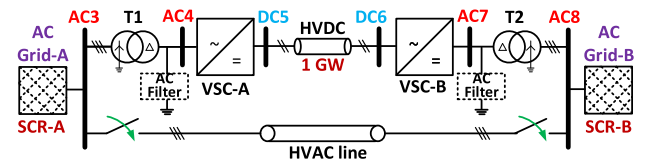
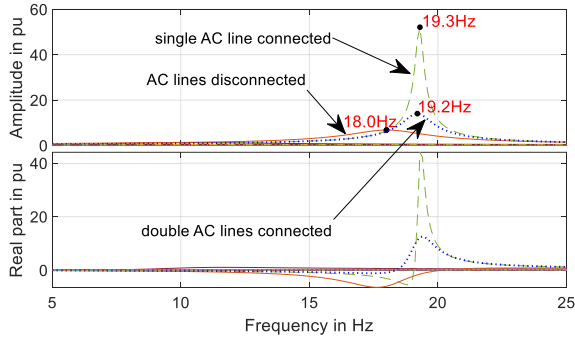**FIGURE 8.** Simplification to the test grid in Fig.1: replacing AC Grid-A with a Thevenin circuit.

FIGURE 9. Modal impedances of the system by: no parallel AC line (solid line), single AC line (dashed line), double AC line (dotted line).
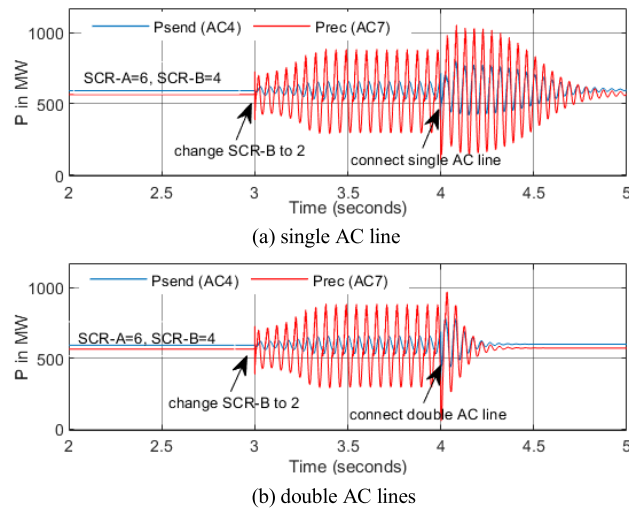

(a) single AC line

(b) double AC lines

FIGURE 10. Stability impact of the parallel AC line in EMT simulation.

TABLE 5. PFs (%) of the 18 Hz mode for different AC line cases.

PF in %	AC3-d/q	AC4-d/q	DC5	DC6	AC7-d/q	AC8-d/q
No	0.4 / 0.1	1.2 / 0.34	5.3	5	**32.7** / 23.3	**18.5** / 13.2
Single	5.3 / **7.6**	5.4 / **14.3**	2.5	2.2	16.9 / **21**	11.4 / **13.4**
Double	6.7 / **8.9**	7.2 / **16.6**	2.6	2.3	15.6 / **18.4**	10 / **11.7**

AC line connection; (c) double AC line connection. All the scenarios have SCR-A=6, SCR-B=2 and U_{dc0} compensation mode for VSC-A. Note that all the SCR values in the paper refer to the HVDC capacity. In Scenario (a), the 18 Hz resonance mode is still unstable due to the negative damping as indicated in the impedance real part plot, while in

Scenarios (b) and (c), the system is stabilized by connecting the parallel AC line(s). In comparison to Scenario (c), the resonance peak in Scenario (b) is much sharper, which indicates a smaller damping ratio according to (4). The 7 Hz resonance mode observed in Section IV.A and IV.B disappears because the AC Grid-A is strengthened. Above analytical results are then validated by the EMT simulation results as shown in Figure 10. The PFs of DC grid nodes as presented in TABLE 5 shows that the AC-DC dynamic coupling in HVDC is weakened by the parallel AC line in this case.
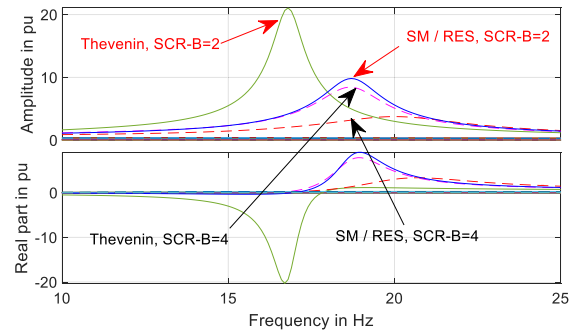
FIGURE 11. Modal impedances when AC Grid-A is modelled as thevenin circuit with SCR-A=2.8 or as SM and RES.
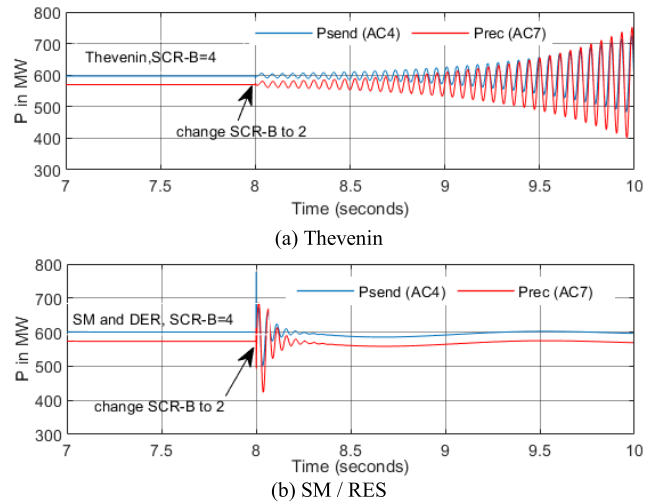
(a) Thevenin

(b) SM / RES

FIGURE 12. EMT simulations with different models of AC Grid-A.

TABLE 6. PFs (%) of the 18 Hz mode for SCR-B=2 and different AC Grid-A models.

AC1-d/q	AC2-d/q	AC3-d/q	AC4-d/q	DC5	DC6	AC7-d/q	AC8-d/q
Thevenin circuit							
		7.6 / 7.4	7.5 / **12**	6.4	5.4	**24** / **11.5**	**10.5** / 7.8
SM / RES							
1.1 / 1.4	4.4 / 4.5	7.1 / 9	6.5 / **14.9**	2.2	1.9	**12.7**/**14.8**	**9.1** / **10.5**

D. STABILITY IMPACT OF SM AND RES
In above analysis, the left and right side external grids are both modelled as Thevenin circuits. To create a more practical

impedance profile, the AC Grid-A is replaced by SM and RES (see Figure 1). And the influence of replacing the Thevenin circuit (with SCR-A=2.8) with SM and RES (in total of 2.8 GVA capacity) is analyzed for the scenarios of varying SCR-B from 4 to 2. Note that the parallel double AC lines of the HVDC link are kept connected in the system. Figure 11 shows the analytical results. When AC Grid-A is modelled as Thevenin circuit, varying SCR-B from 4 to 2 distabilize the system at the 18 Hz dynamic mode. In comparison to Section IV.C, the strength of AC Grid-A is set as SCR-A=2.8 (unstable) instead of SCR-A=6 (stable). After replacing Thevenin circuit with SM / RES, the variation of SCR-B from 4 to 2 does not destabilize the system. And this stability assessment result is furtherly validated by the EMT simulations as shown in Figure 12. Note that the 7 Hz resonance mode observed in Section IV.A and IV.B has not been observed again as the strength of AC Grid-A has not been decreased down to SCR-A=2 again and the parallel AC lines of HVDC are connected in the system.

For the scenarios with SCR-B=2, the PFs of grid nodes are presented in TABLE 6. After replacing the AC Grid-A (Thevenin circuit) with SM and RES, the left side AC grid has more participation in the 18 Hz dynamic mode as the summed PF of AC1-AC4 becomes larger, while the AC-DC dynamic coupling becomes weaker as indicated by the smaller PFs of the DC grid nodes. Another finding from the PF results is, the SM branch participates several times more than the RES branch in the 18 Hz dynamic mode. If furtherly increasing the RES penetration, the stabilizing effect from SM and RES in this case may become weakened. Further analysis on this effect will be presented in a separate paper.

E. DISCUSSION OF OSCILLATION MITIGATION DESIGN

In above subsections, participation factor analysis for the dynamic modes of a simple AC/DC grid was conducted considering different stability impacts. According to the results in TABLE 4 - TABLE 6, the grid nodes AC3 and AC4 have the dominating PFs for the around 7 Hz dynamic mode and the grid nodes AC7 and AC8 have the dominating PFs for the around 18 Hz dynamic mode in most grid conditions as shown in Figure 1, Figure 5 and Figure 8, thus an oscillation mitigation scheme might be preferably configured at these grid nodes [9]. A very effective way is to add active damping control in the HVDC converters at AC3 and AC7, so that no additional passive or active damping devices should be installed there [7], [20]. Moreover, proper damping design in HVDC converters can de-risk the potential oscillation stability for a wide frequency range until the limits of their PWM modulation capability are reached [8], [32], [33].

Apart from the mitigation design in HVDC converters, the damping capability of the RES at AC3, i.e. the active damping in the VSM control scheme here, could also be fully deployed to furtherly increase the overall damping level of the system [29]. However, careful design should be conducted to prevent potential control interactions.

V. CONCLUSION

A straightforward nodal admittance matrix based method, that integrates the detailed dynamics of AC and DC grids as well as AC-DC dynamic coupling, is proposed to assess the stability of converter-interfaced hybrid AC/DC grids. The proposed method not only prevents knowing the number of RHP poles of system minor loop gain as required by Nyquist based method, but also helps identify dynamic modes and PFs of grid components. It is especially advantageous compared to state-space based method, because it does not strictly rely on white-box models, the partial admittance models can also be measured or obtained from product vendors.

The effectiveness of the proposed method is illustrated by case studies with a simple hybrid AC/DC grid consisting embedded HVDC, SM and RES. The stability impacts of varying grid strengths, converter DC voltage compensation mode and switching states of parallel AC line as well as the model variation of AC Grid-A are analyzed. Influences on the AC-DC dynamic coupling are analyzed through grid node PF analysis. It is shown, the GFL controlled HVDC faces potential resonance risk from weak grid connection, and the observed AC-DC dynamic coupling from HVDC converters can introduce the interaction of the connected AC grids. Besides, modelling the connected AC grid of an HVDC converter as simplified Thevenin circuit greatly changes the stability assessment result compared to detailed AC grid model. Moreover, the GFL and GFM converters and SM can operate stably in the considered conditions, and the SM branch participates more than the VSM-controlled RES branch in stabilizing the system in the case study.

In the future, highly meshed AC/DC grids are expected, and the AC-DC dynamic coupling effect is expected to get stronger when HVDC is configured with GFM control (due to the conflict between AC side power availability and DC voltage control) or in a multi-terminal HVDC system with drooped DC voltage control. Moreover, the ever-growing complexity of DC grid may introduce new dynamic modes and/or potentially have larger impact on the dynamic modes which are presently dominated by AC grid, i.e. some dynamic mode could be simultaneouly dominated by both AC and DC grid nodes. The proposed method could be used to analyze the stability risks from such configurations. Furthermore, as the study case is a small system, whether there is any limitation of the proposed method from system size or not would be addressed in future works.

APPENDIX A
SM MODEL

A round rotor SM is considered. The machine has one damping winding in the direct-axis (subscript D) and two damping windings in the quadrature-axis (subscript Q1 and Q2). The field winding is oriented in the direct-axis. When parameterized with fundamental parameters and written in per-unit form, the flux equations of the SM can be formulated as (8), shown at the bottom of the next page, where ω_b and ω denote the base and rotor angular frequency, the subscripts d,

q represent stator d-axis and q-axis under the rotating rotor dq-frame, D, Q denote rotor direct- and quadrature-axis, f denotes the field winding in direct-axis, L_d and L_q are synchronous inductances, L_f, L_D, L_{Q1} and L_{Q2} are the self-inductances of the field winding and damper windings in direct and quadrature axes, L_{ad} and L_{aq} are d and q axis mutual inductances, which satisfy $L_d = L_\sigma + L_{ad}$, $L_q = L_\sigma + L_{aq}$ and $L_f = L_{fd} + L_{ad}$, with L_σ denoting stator leakage inductance and L_{fd} denoting rotor field circuit inductance. The swing and electrical torque equations in per-unit form are:

$$J\dot{\omega} = T_m - T_e - D\omega, \ \dot{\theta} = \omega_b (\omega - \omega_0), \ T_e = \psi_d i_q - \psi_q i_d \tag{9}$$

where T_e and T_m are the electrical and mechanical torques, θ is the rotor angle, and ω_0 is the per-unit steady-state frequency. On the basis that the prime-mover's speed governor is slow compared to the fast transients under consideration, T_m is assumed to be constant. Moreover, the exciter and power system stabilizer (PSS) dynamics are disregarded, resulting a constant field voltage u_f, if desired, these dynamics can be included in the model [34]. Then performing small-signal analysis to (8) and (9), rewriting them in Laplace-form and solving rotor speed dynamic from the swing and electrical torque equations yield

$$\Delta u_s = -Z_{ss}\Delta i_s - \Delta\omega L_{ss}i_{s0} + Z_{sr}\Delta i_r + \Delta\omega L_{sm}i_{r0}$$
$$0 = -Z_{rs}\Delta i_s + Z_{rr}\Delta i_r$$
$$\Delta\omega = -G_m i_{s0}^T \left(C_2 + 2L_{sm}Z_{rr}^{-1}Z_{rs}\right)\Delta i_s \tag{10}$$

where Z_{ss}, Z_{sr}, Z_{rr}, and Z_{rs}, as shown at the bottom of the next page, the symbol Δ denotes small-signal value, $\Delta u_s = \begin{bmatrix} \Delta u_d & \Delta u_q \end{bmatrix}^T$ and $\Delta i_s = \begin{bmatrix} \Delta i_d & \Delta i_q \end{bmatrix}^T$ denote the column vectors of stator small-signal voltages and currents, $\Delta i_r = \begin{bmatrix} \Delta i_f & \Delta i_D & \Delta i_{Q1} & \Delta i_{Q2} \end{bmatrix}^T$ denotes the column vector of rotor small-signal currents, i_{s0} and i_{r0} are the steady-state values of i_s and i_r. Jointly solving the small-signal equations in (10) gives the SM impedance under local rotor rotating dq-frame

$$\Delta u_s = -Z_{dq}^r \Delta i_s$$
$$Z_{dq}^r = Z_{ss} - Z_{sr}Z_{rr}^{-1}Z_{rs}$$
$$\qquad + G_m i_{s0}^T \left(C_2 + 2L_{sm}Z_{rr}^{-1}Z_{rs}\right)(L_{sm}i_{r0} - L_{ss}i_{s0}) \tag{11}$$

Then Z_{dq}^r is furthermore transformed to the local steady-state dq-frame through rotating back the angle deviation δ_0 between rotor and stator, as formulated in

$$Z_{dq} = T_{dq}^{-1}Z_{dq}^r T_{dq} \text{ with } T_{dq} = \frac{1}{\sqrt{2}}\begin{bmatrix} \cos\delta_0 & \sin\delta_0 \\ -\sin\delta_0 & \cos\delta_0 \end{bmatrix} \tag{12}$$

where Z_{dq} is the SM output impedance under system dq-frame. The corresponding admittance can be simply obtained by matrix inversion. The linearized impedance model is then validated using detailed time-domain model from MATLAB/ Simscape, the validation results are omitted for saving sapce. The adopted standard parameters, as given in TABLE 7, can be transformed to the fundamental parameters as used in the derived model according to [35].

TABLE 7. SM standard parameters in per-unit values.

Voltage / Capacity: 27 kV / 1.4 GVA (base system), $J = 10$ s, $D = 0.01$
$X_d = 2.63, X_q = 2.57, X_d' = 0.34, X_q' = 0.54, X_d'' = 0.26, X_q'' = 0.27, X_\sigma = 0.228$
$R_s = 0.0021$, $T_d' = 0.778, T_q' = 0.165, T_d'' = 0.016, T_q'' = 0.016$

APPENDIX B
RES MODEL
The VSM model in [29] is applied for the RES generation, as shown in Figure 3. The VSM is composed of a VSM core, a virtual circuit and an active damping. The VSM core is used to provide a reference for the inner source voltage. The virtual circuit introduces a virtual impedance in series to the RES output filter, which increases the damping of the dynamic modes around nominal frequency. The active damping employs a lead-lag filter to counteract the high-frequency LC oscillation from the AC filter.

The instantaneous power measured with phase (abc) quantities is equivalent to

$$p = i_d u_d + i_q u_q, q = i_d u_q - i_q u_d \tag{13}$$

where $u_{dq} = \begin{bmatrix} u_d & u_q \end{bmatrix}^T$ and $i_{dq} = \begin{bmatrix} i_d & i_q \end{bmatrix}^T$ are the column vectors of the system dq-frame current and voltages. The Q & V droop control in VSM core is deactivated by setting $k_v = 0$. Linearizing the active power equation for the operating point $u_0 = \begin{bmatrix} U_{d0} & U_{q0} \end{bmatrix}^T$ and $i_0 = \begin{bmatrix} I_{d0} & I_{q0} \end{bmatrix}^T$ yields

$$\Delta p = i_0^T \Delta u_{dq} + u_0^T \Delta i_{dq} \tag{14}$$

$$\begin{cases} u_d = -R_s i_d + \dot{\psi}_d/\omega_b - \omega\psi_q \\ u_q = -R_s i_q + \dot{\psi}_q/\omega_b + \omega\psi_d \\ u_f = R_f i_f + \dot{\psi}_f/\omega_b \\ 0 = R_D i_D + \dot{\psi}_D/\omega_b \\ 0 = R_{Q1} i_{Q1} + \dot{\psi}_{Q1}/\omega_b \\ 0 = R_{Q2} i_{Q2} + \dot{\psi}_{Q2}/\omega_b \end{cases} \quad \begin{cases} \psi_d = -L_d i_d + L_{ad} i_f + L_{ad} i_D \\ \psi_q = -L_q i_q + L_{aq} i_{Q1} + L_{aq} i_{Q2} \\ \psi_f = -L_{ad} i_d + L_f i_f + L_{ad} i_D \\ \psi_D = -L_{ad} i_d + L_{ad} i_f + L_D i_D \\ \psi_{Q1} = -L_{aq} i_q + L_{Q1} i_{Q1} + L_{aq} i_{Q2} \\ \psi_{Q2} = -L_{aq} i_q + L_{aq} i_{Q1} + L_{Q2} i_{Q2} \end{cases} \tag{8}$$

Then linearizing the swing equation

$$\omega = (P^{\text{ref}} - p - p_{\text{Pf}})/(T_{\text{AI}}s), \quad p_{\text{Pf}} = k_{\text{Pf}}(\omega - \omega^{\text{ref}})$$
$$\theta = \omega\omega_{\text{b}}/s + k_{\text{Df}}\omega_{\text{b}}(\omega - \omega^{\text{ref}}) \quad (15)$$

and substituting Δp into it leads to

$$\Delta\theta = G_{\text{SYNC}}\left(i_0^{\text{T}}\Delta u_{\text{dq}} + u_0^{\text{T}}\Delta i_{\text{dq}}\right),$$
$$G_{\text{SYNC}} = \frac{-\omega_{\text{b}}(1 + k_{\text{Df}}s)}{s(T_{\text{A}}s + k_{\text{Pf}})} \quad (16)$$

Note that the P / f droop control is configured to work under the limited frequency sensitive mode at over frequency (LFSM-O). When the frequency is within 50.2 Hz, this control function is not activated, thus can be considered as $k_{\text{Pf}} = 0$. Then performing small-signal analysis to the inner voltage control, virtual circuit and active damping branches yields

$$\Delta m_{\text{dq}}^{\text{c}} = \Delta e_{\text{dq}} - G_{\text{vc}}\Delta i_{\text{dq}}^{\text{c}} + G_{\text{ad}}\Delta u_{\text{dq}}^{\text{c}}$$

$$G_{\text{ad}} = k_{\text{ad}}\frac{s + \omega_{\text{lead}}}{s + \omega_{\text{lag}}}, \quad G_{\text{vc}} = \frac{\tau_{\text{rv}}s}{1 + \tau_{\text{rv}}s}\begin{bmatrix} r_{\text{v}} & 0 \\ 0 & r_{\text{v}} \end{bmatrix}$$

$$-\begin{bmatrix} 0 & x_{\text{v}} \\ -x_{\text{v}} & 0 \end{bmatrix} \quad (17)$$

where the superscript c indicates the variables under control dq-frame. The transformation between control dq-frame and system dq-frame can be illustrated by

$$\begin{bmatrix} x_{\text{d}}^{\text{c}} \\ x_{\text{q}}^{\text{c}} \end{bmatrix} = \begin{bmatrix} \cos(\Delta\theta) & \sin(\Delta\theta) \\ -\sin(\Delta\theta) & \cos(\Delta\theta) \end{bmatrix}\begin{bmatrix} x_{\text{d}} \\ x_{\text{q}} \end{bmatrix} = T_{\Delta\theta}\begin{bmatrix} x_{\text{d}} \\ x_{\text{q}} \end{bmatrix} \quad (18)$$

where the angle deviation $\Delta\theta$ equals to the VSM core angle θ minus the grid voltage angle θ_0. Applying this transformation to current, voltage and modulation index yields

$$\begin{cases} \Delta m_{\text{dq}} = -C_2 m_0 \Delta\theta + \Delta m_{\text{dq}}^{\text{c}} \\ \Delta u_{\text{dq}}^{\text{c}} = C_2 u_0 \Delta\theta + \Delta u_{\text{dq}} \\ \Delta i_{\text{dq}}^{\text{c}} = C_2 i_0 \Delta\theta + \Delta i_{\text{dq}} \end{cases} \quad C_2 = \begin{bmatrix} 0 & 1 \\ -1 & 0 \end{bmatrix} \quad (19)$$

where m_0 denotes the steady state values of m_{dq}^{c}, and u_0 and i_0 follow the same notations. Then the power-stage small-signal equation can be written as

$$\underbrace{\frac{e^{-0.5T_{\text{s}}s}(1 - e^{-T_{\text{s}}s})}{T_{\text{s}}s}}_{G_{\text{D}}}\Delta m_{\text{dq}} - \Delta u_{\text{dq}}$$

$$= \underbrace{\begin{bmatrix} R_{\text{c}} + sL_{\text{c}}/\omega_{\text{b}} & -L_{\text{c}} \\ L_{\text{c}} & R_{\text{c}} + sL_{\text{c}}/\omega_{\text{b}} \end{bmatrix}}_{Z_{\text{RL}}}\Delta i_{\text{dq}} \quad (20)$$

where G_{D} models the control delay and sampling process. Jointly solving the above linearized equations yields (21), as shown at the bottom of the page, where $g_{2\times 1} = G_{\text{D}}(G_{\text{ad}}C_2 u_0 - G_{\text{vc}}C_2 i_0 - C_2 m_0)$.

TABLE 8. Parameters of the aggregated VSM-controlled RES.

Voltage / Capacity	650 V(AC) /1800 V(DC) / 1.4 GVA (base system for
AC circuits	$R_{\text{c}} = 8.5\ \mu\Omega$, $L_{\text{c}} = 0.085\ \mu\text{H}$, $R_{\text{f}} = 0.85\ \mu\Omega$, $C_{\text{f}} = 0.2769$ F
VSM core	$k_{\text{Pf}} = 20$, $k_{\text{Df}} = 0.125$, $T_{\text{A}} = 10$, $k_{\text{v}} = 0$, $T_{\text{v}} = 1$
Virtual circuit	$r_{\text{v}} = 0.13$, $x_{\text{v}} = 0.11$, $\tau_{\text{rv}} = 0.008$
Active damping	$k_{\text{ad}} = 1$, $\omega_{\text{lead}} = 0$, $\omega_{\text{lag}} = 1500 \cdot 2\pi$

The derived output impedance of VSM under system dq-frame Z_{dq} is validated using detailed nonlinear EMT model with the parameters as given in TABLE 8. Due to space reason, the validation results are not presented here.

$$Z_{\text{ss}} = \begin{bmatrix} R_{\text{s}} + L_{\text{d}}s/\omega_{\text{b}} & -\omega_0 L_{\text{q}} \\ \omega_0 L_{\text{d}} & R_{\text{s}} + L_{\text{q}}s/\omega_{\text{b}} \end{bmatrix}, \quad L_{\text{sm}} = \begin{bmatrix} 0 & 0 & -L_{\text{aq}} & -L_{\text{aq}} \\ L_{\text{ad}} & L_{\text{ad}} & 0 & 0 \end{bmatrix}$$

$$Z_{\text{sr}} = \begin{bmatrix} L_{\text{ad}}s/\omega_{\text{b}} & L_{\text{ad}}s/\omega_{\text{b}} & -\omega_0 L_{\text{aq}} & -\omega_0 L_{\text{aq}} \\ \omega_0 L_{\text{ad}} & \omega_0 L_{\text{ad}} & L_{\text{aq}}s/\omega_{\text{b}} & L_{\text{aq}}s/\omega_{\text{b}} \end{bmatrix}, \quad L_{\text{ss}} = \begin{bmatrix} 0 & -L_{\text{q}} \\ L_{\text{d}} & 0 \end{bmatrix}$$

$$Z_{\text{rr}} = \begin{bmatrix} R_{\text{f}} + L_{\text{f}}s/\omega_{\text{b}} & L_{\text{ad}}s/\omega_{\text{b}} & 0 & 0 \\ L_{\text{ad}}s/\omega_{\text{b}} & R_{\text{D}} + L_{\text{D}}s/\omega_{\text{b}} & 0 & 0 \\ 0 & 0 & R_{\text{Q1}} + L_{\text{Q1}}s/\omega_{\text{b}} & L_{\text{aq}}s/\omega_{\text{b}} \\ 0 & 0 & L_{\text{aq}}s/\omega_{\text{b}} & R_{\text{Q2}} + L_{\text{Q2}}s/\omega_{\text{b}} \end{bmatrix}$$

$$Z_{\text{rs}} = \begin{bmatrix} L_{\text{ad}}s/\omega_{\text{b}} & 0 \\ L_{\text{ad}}s/\omega_{\text{b}} & 0 \\ 0 & L_{\text{aq}}s/\omega_{\text{b}} \\ 0 & L_{\text{aq}}s/\omega_{\text{b}} \end{bmatrix}, \quad G_{\text{m}} = \frac{1}{Js + D}, \quad C_2 = (L_{\text{q}} - L_{\text{d}})\begin{bmatrix} 0 & 1 \\ 1 & 0 \end{bmatrix}$$

$$\Delta u_{\text{dq}} = -\underbrace{\left((1 - G_{\text{D}}G_{\text{ad}})I_2 - G_{\text{SYNC}}g_{2\times 1}i_0^{\text{T}}\right)^{-1}\left(Z_{\text{RL}} + G_{\text{D}}G_{\text{vc}} - G_{\text{SYNC}}g_{2\times 1}u_0^{\text{T}}\right)}_{Z_{\text{dq}}}\Delta i_{\text{dq}} \quad (21)$$

APPENDIX C
HVDC CONVERTER MODEL

Circuit and control diagrams of HVDC converters are shown in Figure 4. For both converters, the transfer function of the standard SRF-PLL is

$$\theta_{\text{PLL}} = \omega_{\text{PLL}}/s = u_q^c H_{\text{PLL}}(s)/s \qquad (22)$$

where $H_{\text{PLL}}(s)$ denotes the transfer function of the PI controller in PLL. Assuming a small-signal perturbation $\Delta\theta_{\text{PLL}}$ on the PLL angle, the variables in system dq-frame can be rotated to the control dq-frame by multiplying

$$T_{\Delta\theta_{\text{PLL}}} = \begin{bmatrix} \cos(\Delta\theta_{\text{PLL}}) & \sin(\Delta\theta_{\text{PLL}}) \\ -\sin(\Delta\theta_{\text{PLL}}) & \cos(\Delta\theta_{\text{PLL}}) \end{bmatrix}$$
$$\approx \begin{bmatrix} 1 & \Delta\theta_{\text{PLL}} \\ -\Delta\theta_{\text{PLL}} & 1 \end{bmatrix} \qquad (23)$$

Then we will have

$$u_{\text{dq}}^c = T_{\Delta\theta_{\text{PLL}}} u_{\text{dq}}, i_{\text{dq}}^c = T_{\Delta\theta_{\text{PLL}}} i_{\text{dq}}, m_{\text{dq}} = T_{\Delta\theta_{\text{PLL}}}^{-1} m_{\text{dq}}^c \qquad (24)$$

Performing small-signal analysis to above equations and jointly solving them yields

$$\Delta\theta = G_{\text{PLL}}\Delta u_q, G_{\text{PLL}} = H_{\text{PLL}}/(s + U_{d0}H_{\text{PLL}}),$$
$$\Delta u_{\text{dq}}^c = G_{\text{PLL}}^u \Delta u_{\text{dq}}$$
$$\Delta i_{\text{dq}}^c = G_{\text{PLL}}^i \Delta u_{\text{dq}} + \Delta i_{\text{dq}}, \Delta m_{\text{dq}} = G_{\text{PLL}}^m \Delta u_{\text{dq}} + \Delta m_{\text{dq}}^c \qquad (25)$$

$$G_{\text{PLL}}^u = \begin{bmatrix} 1 & U_{q0}G_{\text{PLL}} \\ 0 & 1 - U_{d0}G_{\text{PLL}} \end{bmatrix}, G_{\text{PLL}}^i = \begin{bmatrix} 0 & I_{q0}G_{\text{PLL}} \\ 0 & -I_{d0}G_{\text{PLL}} \end{bmatrix},$$
$$G_{\text{PLL}}^m = \begin{bmatrix} 0 & -M_{q0}G_{\text{PLL}} \\ 0 & M_{d0}G_{\text{PLL}} \end{bmatrix} \qquad (26)$$

where $U_{d0}, U_{q0}, I_{d0}, I_{q0}, M_{d0}, M_{q0}$ denote the steady state voltages, currents and modulation indexes and can be written in vector form as

$$u_0 = \begin{bmatrix} U_{d0} & U_{q0} \end{bmatrix}^T, u_0 = \begin{bmatrix} I_{d0} & I_{q0} \end{bmatrix}^T, u_0 = \begin{bmatrix} M_{d0} & M_{q0} \end{bmatrix}^T \qquad (27)$$

The power-stage and control equations can be written in small-signal form as

$$\Delta u_{\text{c,dq}} - \Delta u_{\text{dq}} = Z_{\text{RL}}\Delta i_{\text{dq}}$$
$$\Delta m_{\text{dq}}^c = H_{\text{CC}}\Delta i_{\text{dq}}^{\text{ref}} - G_{\text{CC}}\Delta i_{\text{dq}}^c, G_{\text{CC}} = \begin{bmatrix} H_{\text{CC}} & K_d \\ -K_d & H_{\text{CC}} \end{bmatrix} \qquad (28)$$

where H_{CC} describes the current PI controller and $u_{\text{c,dq}}$ describes the modulated converter voltage as represented by

$$u_{\text{c,dq}} = G_D m_{\text{dq}} u_{\text{dc}}/u_{\text{dc}} = G_D m_{\text{dq}}$$
$$u_{\text{c,dq}} = G_D m_{\text{dq}} u_{\text{dc}}/U_{\text{dc0}} \qquad (29)$$

for the u_{dc} and U_{dc0} compensation mode respectively. Linearizing them leads to

$$\Delta u_{\text{c,dq}} = G_D\Delta m_{\text{dq}}, \Delta u_{\text{c,dq}} = G_D\Delta m_{\text{dq}} + G_D m_0\Delta u_{\text{dc}}/U_{\text{dc0}} \qquad (30)$$

Then assuming an AC-DC power lossless conversion, we have

$$p = i_d u_{\text{cd}} + i_q u_{\text{cq}} = i_{\text{dq}}^T u_{\text{c,dq}} = i_{\text{dc}} u_{\text{dc}} - 0.5 C_{\text{dc}} u_{\text{dc}}^2 s/\omega_b \qquad (31)$$

which can be linearized to

$$i_0^T\Delta u_{\text{c,dq}} + u_{c0}^T\Delta i_{\text{dq}} = \Delta i_{\text{dc}} U_{\text{dc0}} + I_{\text{dc0}}\Delta u_{\text{dc}}$$
$$- C_{\text{dc}} U_{\text{dc0}}\Delta u_{\text{dc}} s/\omega_b \qquad (32)$$

Fort the power control mode converter, it is set $\Delta i_{\text{dq}}^* = 0$. For the voltage control mode converter, the current reference dynamics can be written as

$$\begin{bmatrix} \Delta i_d^{\text{ref}} \\ \Delta i_q^{\text{ref}} \end{bmatrix} = \begin{bmatrix} 0_{1\times 2} \\ -H_{\text{Vac}}u_0^T G_{\text{PLL}}^u \end{bmatrix}\Delta u_{\text{dq}} + \begin{bmatrix} H_{\text{vdc}} \\ 0 \end{bmatrix}\Delta u_{\text{dc}}$$
$$= A_2\Delta u_{\text{dq}} + b_{2\times 1}\Delta u_{\text{dc}} \qquad (33)$$

where H_{Vdc} and H_{Vac} describe a PI controller and a PT1 element respectively. Combining the above equations, the relation between AC ports and DC port variables under instantaneous DC voltage (u_{dc}) compensation can be solved as

$$\begin{bmatrix} -\Delta i_{\text{dq}} \\ \Delta i_{\text{dc}} \end{bmatrix} = \begin{bmatrix} Y_{\text{dqdq}} & y_{\text{dqdc}} \\ y_{\text{dcdq}} & Y_{\text{dcdc}} \end{bmatrix}\begin{bmatrix} \Delta u_{\text{dq}} \\ \Delta u_{\text{dc}} \end{bmatrix}$$
$$= \begin{bmatrix} Y_{\text{dd}} & Y_{\text{dq}} & Y_{\text{ddc}} \\ Y_{\text{qd}} & Y_{\text{qq}} & Y_{\text{qdc}} \\ Y_{\text{dcd}} & Y_{\text{dcq}} & Y_{\text{dcdc}} \end{bmatrix}\begin{bmatrix} \Delta u_{\text{dq}} \\ \Delta u_{\text{dc}} \end{bmatrix} \qquad (34)$$

where I_2 denotes the second-order identity matrix and

$$Y_{\text{dqdq}} = (Z_{\text{RL}} + G_D G_{\text{CC}})^{-1}(I_2 - G_D(G_{\text{PLL}}^m - G_{\text{CC}}G_{\text{PLL}}^i))$$
$$y_{\text{dqdc}} = \begin{bmatrix} 0 & 0 \end{bmatrix}^T$$
$$y_{\text{dcdq}} = (i_0^T - (i_0^T Z_{\text{RL}} + m_0^T G_D)Y_{\text{dq}})/U_{\text{dc0}}$$
$$Y_{\text{dcdc}} = -I_{\text{dc0}}/U_{\text{dc0}} + C_{\text{dc}}s/\omega_b \qquad (35)$$

for the power control mode converter while

$$Y_{\text{dqdq}} = (Z_{\text{RL}} + G_D G_{\text{CC}})^{-1}(I_2 - G_D(G_{\text{PLL}}^m$$
$$+ H_{\text{CC}}A_2 - G_{\text{CC}}G_{\text{PLL}}^i))$$
$$y_{\text{dqdc}} = -(Z_{\text{RL}} + G_D G_{\text{CC}})^{-1} G_D H_{\text{CC}}b_{2\times 1}$$
$$y_{\text{dcdq}} = (i_0^T - (i_0^T Z_{\text{RL}} + m_0^T G_D)Y_{\text{dq}})/U_{\text{dc0}}$$
$$Y_{\text{dcdc}} = -((i_0^T Z_{\text{RL}} + m_0^T G_D)y_{\text{dqdc}} + I_{\text{dc0}})/U_{\text{dc0}} + C_{\text{dc}}s/\omega_b \qquad (36)$$

for the voltage control mode converter. Comparing (35) and (36), the power control mode has weaker AC-DC coupling than the voltage control mode converter. However, if replacing u_{dc} compensation with constant DC voltage (U_{dc0}) compensation in the power control mode converter, we have

$$y_{\text{dqdc}} = -(Z_{\text{RL}} + G_D G_{\text{CC}})^{-1} m_0/U_{\text{dc0}}$$
$$Y_{\text{dcdc}} = -((i_0^T Z_{\text{RL}} + m_0^T G_D)y_{\text{dqdc}} + I_{\text{dc0}})/U_{\text{dc0}} + C_{\text{dc}}s/\omega_b \qquad (37)$$

which strengthens the AC-DC coupling. Similarly, the admittance model of the voltage control mode converter can be adapted for U_{dc0} compensation. Note that the per-unit base system for the AC and DC pu quantities of above models are chosen in the way to achieve invariant AC-DC power transformation [7]. Using the parameters as given in TABLE 9, the three-port admittance model in (34) is validated through EMT simulation.

TABLE 9. Parameters of HVDC converters.

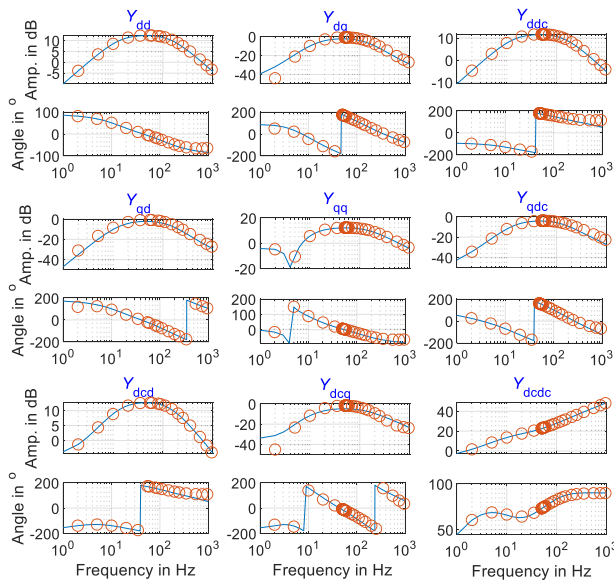| HVDC converter VSC-A	
AC circuits	$R_c = 0.45\ \Omega$, $L_c = 0.143$ mH, $R_f = 0.45\ \Omega$, $C_f = 522$ nF
Current control	$H_{CC} = 0.422 + 39.38\,/\,s$, $K_d = L_c$
PLL PI controller	$H_{PLL} = 50 + 625\,/\,s$ (same for VSC-B)
DC capacitor	$C_{DC} = 50\ \mu$F (same for VSC-B)
HVDC converter VSC-B	
AC circuits	$R_c = 0.45\ \Omega$, $L_c = 0.143$ mH, $R_f = 0.45\ \Omega$, $C_f = 522$ nF
Current control	$H_{CC} = 0.422 + 39.38\,/\,s$, $K_d = L_c$
Voltage control	$H_{Vdc} = 15 + 1050\,/\,s$, $H_{Vac} = -5\,/\,(1 + 0.01s)$

FIGURE 13. Comparison of HVDC converter admittance response from EMT simulation (circles) and the analytical admittance model (solid line).

As an example, the validation of the power control model converter with U_{dc0} compensation is presented in Figure 13. The impedance amplitudes are shown in dB of Ohms and the impedance angles are shown in degrees, as denoted by '$\circ$'. The observed error around 2 Hz may come from the inaccurate frequency extraction. As the low frequency near 0 Hz in dq-frame corresponds to a frequency around the nominal grid frequency 50 Hz in the phase or sequence domain. It is difficult to accurately extract a small-signal frequency component near 50 Hz from a measured signal dominated by the fundamental frequency component.

REFERENCES

[1] X. Liu, "Control of voltage source converter based high voltage direct current transmission systems for grid code compliance," Ph.D. dissertation, Inst. Electr. Power Syst., Otto von Guericke Univ. Magdeburg, Magdeburg, Germany, 2016.

[2] S. Raths, D. Beck, T. Bongers, and I. Sander, "ALEGrO—Market integration und system operation aspects of the new HVDC link between Germany and Belgium," in *Proc. ETG Congr.*, 2021, pp. 1–6.

[3] C. Buchhagen, C. Rauscher, A. Menze, and J. Jung, "BorWin1—First experiences with harmonic interactions in converter dominated grids," in *Proc. Int. ETG Congr.*, 2015, pp. 1–7.

[4] C. Buchhagen, M. Greve, A. Menze, and J. Jung, "Harmonic stability—Practical experience of a TSO," in *Proc. 15th Wind Integr. Workshop*, 2016, pp. 1–6.

[5] X. Wang and F. Blaabjerg, "Harmonic stability in power electronic-based power systems: Concept, modeling, and analysis," *IEEE Trans. Smart Grid*, vol. 10, no. 3, pp. 2858–2870, May 2019.

[6] C. Yin, X. Xie, S. Xu, and C. Zou, "Review of oscillations in VSC-HVDC systems caused by control interactions," *J. Eng.*, vol. 2019, no. 16, pp. 1204–1207, Mar. 2019.

[7] Y. Zhang, "Analysis and control of resonances in HVDC connected DFIG-based offshore wind farm," Ph.D. dissertation, Inst. Electr. Power Syst., Otto von Guericke Univ. Magdeburg, Magdeburg, Germany, 2021.

[8] C. Zou, H. Rao, S. Xu, Y. Li, W. Li, J. Chen, X. Zhao, Y. Yang, and B. Lei, "Analysis of resonance between a VSC-HVDC converter and the AC grid," in *Proc. IEEE Trans. Power Electron.*, vol. 33, no. 12, pp. 10157–10168, Dec. 2018.

[9] Y. Zhang, C. Klabunde, and M. Wolter, "Harmonic filtering in DFIG-based offshore wind farm through resonance damping," in *Proc. IEEE PES Innov. Smart Grid Technol. Eur. (ISGT-Europe)*, Sep. 2019, pp. 1–5.

[10] L. Fan and Z. Miao, "Admittance-based stability analysis: Bode plots, Nyquist diagrams or eigenvalue analysis?" *IEEE Trans. Power Syst.*, vol. 35, no. 4, pp. 3312–3315, Jul. 2020.

[11] O. C. Sakinci and J. Beerten, "Generalized dynamic phasor modeling of the MMC for small-signal stability analysis," *IEEE Trans. Power Del.*, vol. 34, no. 3, pp. 991–1000, Jun. 2019.

[12] K. Ji, G. Tang, J. Yang, Y. Li, and D. Liu, "Harmonic stability analysis of MMC-based DC system using DC impedance model," *IEEE J. Emerg. Sel. Topics Power Electron.*, vol. 8, no. 2, pp. 1152–1163, Jun. 2020.

[13] Y. Chen, L. Xu, A. Egea-Alvarez, B. Marshall, M. H. Rahman, and A. D. Oluwole, "MMC impedance modeling and interaction of converters in close proximity," *IEEE J. Emerg. Sel. Topics Power Electron.*, vol. 9, no. 6, pp. 7223–7236, Dec. 2021.

[14] C. Zhang, M. Molinas, A. Rygg, and X. Cai, "Impedance-based analysis of interconnected power electronics systems: Impedance network modeling and comparative studies of stability criteria," *IEEE J. Emerg. Sel. Topics Power Electron.*, vol. 8, no. 3, pp. 2520–2533, Sep. 2020.

[15] S. Shah and L. Parsa, "Impedance modeling of three-phase voltage source converters in DQ, sequence, and phasor domains," *IEEE Trans. Energy Convers.*, vol. 32, no. 3, pp. 1139–1150, Sep. 2017.

[16] J. Sun, "Two-port characterization and transfer immittances of AC-DC converters—Part I: Modeling," *IEEE Open J. Power Electron.*, vol. 2, pp. 440–462, 2021.

[17] J. Pedra, L. Sainz, and L. Monjo, "Three-port small signal admittance-based model of VSCs for studies of multi-terminal HVDC hybrid AC/DC transmission grids," *IEEE Trans. Power Syst.*, vol. 36, no. 1, pp. 732–743, Jan. 2021, doi: 10.1109/TPWRS.2020.3003835.

[18] H. Zhang, M. Mehrabankhomartash, M. Saeedifard, Y. Zou, Y. Meng, and X. Wang, "Impedance analysis and stabilization of point-to-point HVDC systems based on a hybrid AC–DC impedance model," *IEEE Trans. Ind. Electron.*, vol. 68, no. 4, pp. 3224–3238, Apr. 2021, doi: 10.1109/TIE.2020.2978706.

[19] W. Xu, Z. Huang, Y. Cui, and H. Wang, "Harmonic resonance mode analysis," *IEEE Trans. Power Del.*, vol. 20, no. 2, pp. 1182–1190, Apr. 2005.

[20] Y. Zhang, C. Klabunde, and M. Wolter, "Study of resonance issues between DFIG-based offshore wind farm and HVDC transmission," *Electr. Power Syst. Res.*, vol. 190, Jan. 2021, Art. no. 106767.

[21] F. Thams, R. Eriksson, and M. Molinas, "Interaction of droop control structures and its inherent effect on the power transfer limits in multiterminal VSC-HVDC," *IEEE Trans. Power Del.*, vol. 32, no. 1, pp. 182–192, Feb. 2017, doi: 10.1109/TPWRD.2016.2600028.

[22] R. Bellman, *Introduction to Matrix Analysis*, 2nd ed. New York, NY, USA: McGraw-Hill, 1970.

[23] E. I. Green, "The story of *Q*," *Amer. Scientist*, vol. 43, pp. 584–594, Oct. 1955.

[24] E. Ebrahimzadeh, F. Blaabjerg, X. Wang, and C. L. Bak, "Bus participation factor analysis for harmonic instability in power electronics based power systems," *IEEE Trans. Power Electron.*, vol. 33, no. 12, pp. 10341–10351, Dec. 2018, doi: 10.1109/TPEL.2018.2803846.

[25] G. He, W. Wang, and H. Wang, "Coordination control method for multi-wind farm systems to prevent sub/super-synchronous oscillations," *CSEE J. Power Energy Syst.*, early access, Nov. 13, 2021, doi: 10.17775/CSEE-JPES.2020.06550.

[26] J. Sun, "Frequency-domain stability criteria for converter-based power systems," *IEEE Open J. Power Electron.*, vol. 3, pp. 222–254, 2022, doi: 10.1109/OJPEL.2022.3155568.

[27] B. Gustavsen and A. Semlyen, "Rational approximation of frequency domain responses by vector fitting," *IEEE Trans. Power Del.*, vol. 14, no. 3, pp. 1052–1061, Jul. 1999.

[28] P. Kundur, *Power System Stability and Control*. New York, NY, USA: McGraw-Hill, 1994.

[29] D. Duckwitz, "Power system inertia: Derivation of requirements and comparison of inertia emulation methods for converter-based power plants," Ph.D. dissertation, Dept. Integr. Energy Syst., Universität Kassel und Fraunhofer IEE, Kassel, Germany, 2019.

[30] Y. Zhang, C. Klabunde, and M. Wolter, "Frequency-coupled impedance modeling and resonance analysis of DFIG-based offshore wind farm with HVDC connection," *IEEE Access*, vol. 8, pp. 147880–147894, 2020.

[31] M. Amin and M. Molinas, "Understanding the origin of oscillatory phenomena observed between wind farms and HVDC systems," *IEEE J. Emerg. Sel. Topics Power Electron.*, vol. 5, no. 1, pp. 378–392, Mar. 2017.

[32] J. Lyu, X. Cai, and M. Molinas, "Optimal design of controller parameters for improving the stability of MMC-HVDC for wind farm integration," *IEEE J. Emerg. Sel. Topics Power Electron.*, vol. 6, no. 1, pp. 40–53, Mar. 2018, doi: 10.1109/JESTPE.2017.2759096.

[33] B. Pang, H. Nian, and Y. Xu, "Mechanism analysis and damping method for high frequency resonance between VSC-HVDC and the wind farm," *IEEE Trans. Energy Convers.*, vol. 36, no. 2, pp. 984–994, Jun. 2021, doi: 10.1109/TEC.2020.3023428.

[34] L. Harnefors, "Analysis of subsynchronous torsional interaction with power electronic converters," *IEEE Trans. Power Syst.*, vol. 22, no. 1, pp. 305–313, Feb. 2007.

[35] J. A. Martinez, B. Johnson, and C. Grande-Moran, "Parameter determination for modeling system transients—Part IV: Rotating machines," *IEEE Trans. Power Del.*, vol. 20, no. 3, pp. 2063–2072, Jul. 2005.

DANIEL DUCKWITZ received the Dipl.-Ing. degree in mechatronical engineering from the University of Erlangen–Nueremberg, Erlangen, Germany, in 2010, and the Ph.D. degree in electrical engineering from the University of Kassel, Germany, in 2019. From 2010 to 2021, he has been a Researcher with the Fraunhofer Institute for Energy Economics and Energy System Technology, and from 2019 to 2021, he has been a team leader in the Department of Energy Management and Power System Operation at the University of Kassel. He is currently a Product Manager of grid services with SMA Solar Technology AG.

NILS WIESE received the bachelor's and master's degrees in renewable energy technologies and systems engineering from the Flensburg University of Applied Sciences, Flensburg, Germany, in 2017 and 2019, respectively. He is currently pursuing the Ph.D. degree with the Department of Energy Management and Power System Operation, University of Kassel, Kassel, Germany.

YONGGANG ZHANG (Member, IEEE) received the B.S. degree from Chang'an University, Xi'an, China, in 2007, the M.S. degree from Duisburg-Essen University, Germany, in 2010, and the Ph.D. degree from the Otto-von-Guericke University Magdeburg, Germany, in 2021, all in electrical engineering. He is currently a Postdoctoral Researcher with the Department of Energy Management and Power System Operation, University of Kassel.

MARTIN BRAUN (Senior Member, IEEE) received the Diploma degree in electrical engineering and in technically oriented business administration from the University of Stuttgart, Stuttgart, Germany, in 2005, and the Ph.D. degree in engineering from the University of Kassel, Kassel, Germany, in 2008.

He is currently a Professor with the Department of Energy Management and Power System Operation, University of Kassel, and the Director of the Grid Planning and Grid Operation Division, Fraunhofer Institute for Energy Economics and Energy System Technology, Kassel.

● ● ●